Barber, N.D., Edmonds, M., Jenner, F., and Williams, H., 2022, Global Ba/Nb systematics in arc magmas reflect the depths of mineral dehydration in subducted slabs: Geology, https://doi.org/10.1130/G50447.1

SUPPLEMENTAL FILE 1

COLOR SCHEMES

Many of the color schemes used in our figures (Figs. 2, S4, S6, S7, S8) are sourced from Scientific Color Map 6 (Crameri, 2018). These color map schemes (*vik, turku, greyC, hawaii)* are all color-blind friendly and perceptually uniform. The rest of the color used are default color options in *matplotlib*.

METHODS

The methods employed to compile, condense, and statistically validate this compilation are discussed in Barber et al. (2021), however a summary will be given here. Important data sources informing our compilation are (1) GEOROC for the major igneous geochemical and petrological data (Sarbas and Nohl, 2008), (2) Slab2 for slab geometries and DTS (Hayes et al., 2018), crustal thickness estimates from (Szwillus et al., 2019), and subducting slab sediment cover estimates (Pasyanos et al., 2014). A python script available on GitHub (https://github.com/ndb38/arc-metals) compiled existing GeoRoc data in a self-consistent and structured manner, making a Python-readable CSV master database that formed the basis of later compilation efforts. To complement our previously published datasets (Barber et al., 2021), we integrated an existing thermodynamic dataset (Hernández-Uribe and Palin, 2019) which related major phases and their stability from an N-MORB composition slab (Gale et al., 2013). The published thermodynamic model that we use (Hernández-Uribe and Palin, 2019) employs the thermodynamic software Perple_X to estimate the proportion and stability of major mineral phases in subducting slabs subjected to three different geotherms.

VALIDATION OF BA/NB PEAKS: MONTE CARLO SIMULATIONS

See Supplemental item 2 for a discussion of the modeling strategy that went in to making Figure S7. A summary of our approach and findings will still be provided here. The analyses done to identify the three characteristic Ba/Nb peaks in Figure 1C have been conducted with an eye towards ruling out the effect of other processes; therefore Mg# is reported within each bin, to verify that fractionation doesn't seem to be a control on the observed spread of Ba/Nb contents. However, we can go one step further with this kind of analysis. What Ba/Nb would a magma have if it was melted out of a typical peridotite source, and then fractionally crystallized? Could such a simple melt + fractionation process explains the observed spread in Ba/Nb in Figure 1C?

An alternative way to view these questions is to pose a null hypothesis – Ba/Nb contents in arc magmas are the product of mantle melting and melt fractionation in the absence of any specific slab devolatilization process. While anyone familiar with this field of research will instantly recognize this null hypothesis is false (most arc magmas are generated with a strong fluid component), posing this null hypothesis allows us to qualitatively assess whether the observed Ba/Nb in natural magmas is significantly above "baseline" Ba/Nb contents derived from dry mantle melting and fractionation. If the null hypothesis is shown to be incorrect, then it confirms our observation that these three "peaks" in our data represent real signals of slab devolatilization not previously captured in such a way in the literature.

In order to assess our null hypothesis, we designed a simple simulation using Monte Carlo methods. The approach taken, particularly as it pertains to the parameter space of the simulations, is summarized in Supplementary Information 2. Of relevance here is the fact that we employ modal batch-melting and Rayleigh fractionation as our trace element enrichment models. We performed 10,000 simulations, where the starting [Ba], [Nb], relevant partition coefficients, degree of melting, degree of fractionation, and depth to slab were all varied in a random but uniform and physically realistic parameter space. The results of this simulations are shown as 2D density histograms in Figure S7. The takeaway from this modeling is that the observed median Ba/Nb within each bin in Figure 1C, and even the moving average curve itself lie significantly above the possible parameter space as explained by dry melting and fractionation. Also, our Monte Carlo results show uniform distribution with respect to DTS; in contrast, the natural data (blue curve and blue bins in Figure S7) show non-uniform spatial distributions. In particular, the location of elevated Ba/Nb contents corresponds to a particular DTS, something our spatially invariant Monte Carlo methods do not consider. In all, Figure S7 strengthens our analysis in 1C, demonstrating that the "peaks" identified are real signals on slab devolatilization, as they can't be explained by melting and fractionation processes alone.

VALIDATION OF BA/NB PEAKS: BIN TESTING

A common data visualization tool used to summarize large and complex datasets is binning, whereby the central tendency (either mean, median, or some other statistic) of variable Y is summarized across a discrete (and usually small) interval of variable X. If the X interval chosen for binning is too large, small-scale but important localized structures in the data will be averaged out. However, if the bin size is too small, too much noise will be captured in the bins and the bigger picture signals will be missed. Another common method that tried to get around this problem is employing a moving average – whereby a "box" captures the same number of points repeatedly across an entire figure. Every N number of points, a new value of both X and Y variables are calculated. The size of N determines how "smooth" or how noisy the resulting moving average curve is. Like with binning, if the moving average box size is too large, not enough signal is preserved. Too small, and noise can be mistaken for signal.

We combined the binning and moving average analytical approaches described above to create in Figure 1C, as it allows us to identify areas where Ba/Nb are highest above background (See above section and Figure S7 to understand what we mean by "background") at relatively high data resolution. Ba/Nb contents in arc magmas are widely reported, and thus cover a huge range of values over many tens of kilometers depths to slab. However, as outlined above, the selection of both bin size and moving average box size can and will affect the kinds of signals we see and interpret as important. Therefore, we performed a sensitivity analysis for both bin and box size, reported in Figure S6. In this figure, we show the effect of varying the # of bins from ~ 80 to > 200, and at the same time the effect of varying the moving average box size from N = 5 to N = 30. The analysis we report in the main text and in Figure 1C is marked with a yellow star. As should be evident, this yellow starred analysis represents a reasonable compromise between bin sizes that are too small or too large and moving average boxes that smooth too much or not enough. We see that too many bins make the actual Ba/Nb signals at a given DTS too noisy; the bottom row of Figures where there are over 200 binned median Ba/Nb contents attest to this noisiness. At the same time, too few bins miss the obviously important structure in the data – namely, that arc magmas are only generated at characteristic depths thanks to flux melting. If we make our moving average box size large enough, we can smooth out the presence of the first Ba/Nb peak, and significantly depress the intensity of the 2nd and 3rd Ba/Nb signal. However, such large moving average box sizes seem inappropriate, as they average together disparate magmas at a range of DTS that likely have no petrological affiliation. Similarly, too small of a box means we are overfitting the moving average curve to noise in our bins, rather than the important structures themselves. We believe this sensitivity analysis justifies our choice of bin size and moving average box size, particularly as we wish to capture globally relevant and verifiable process controlling Ba/Nb contents in arc magmas.

GLOBAL FME CONTENTS

The whole rock concentrations of arc magmas included in the *ArcMetal* database ranges from 0 to 2500 ppm for [Ba] (where brackets denote concentrations), 0 to 311 ppm for [Pb] and 0 – 10 ppm for [U] (See Figures S1A-C for summary). Each of these FME are mobile under different conditions and their mobility is best assessed when compared to fluid-immobile elements of similar incompatibility during melting of peridotite and fractional crystallization (Elliott et al., 1997; Pearce et al., 2005). For this study, we employed commonly used ratios like Ba/Nb (Elliott et al., 1997; Pearce et al., 2005) and Th/U (Kelley et al., 2005; Carter et al., 2015). Both metrics have been used to infer the effects of addition of subducting slab sourced fluids and melts to the mantle wedge. We also employ Pb/Nd in this study, which is less commonly used compared to the similar metric Pb/Ce. Both Pb and Nd will behave similarly in a silicate melt, with both having a similar degree of incompatibility (tending to increase with decreasing melt proportion); however unlike Pb, Nd is not significantly fluid mobile, and will therefore not be strongly affected by temperature-induced slab dehydration outside of anomalously Cl-rich brines (Kelley

et al., 2005; Pearce et al., 2005; Rustioni et al., 2019, 2021). Other common geochemical indices in subduction zones like Pb/Ce (William Pitcher and Kent, 2019), while useful, may not provide a simple discrimination between fluid-fluxing and melting, as recent work has found that light rare earth elements like Ce can be mobilized in fluids fluxed from eclogites (Tsay et al., 2017).

The interpretation, usefulness, and limitations of each of these FME ratios will be expanded on below. Figure S1 and S2 show the relative distribution of Ba/Nb, Thu/U, and Pb/Nd in arc magmas globally; these plots demonstrate that the peak values for these metrics are defined by a high degree of variability (Figs S2). This variability sees most of the data captured in the inter-quartile range of each metric, but a significant (> 10%) of the total data falling outside the IQR, skewing towards the right. Pb/Nd is less variable than both Th/U and Ba/Nb overall, but still has a significant number of outliers to the right matching both of the other metrics trends. Because Ba and Nb show similar incompatibilities during fractional crystallization, the Ba/Nb of arc magmas is typically taken to reflect source variability (Elliott et al., 1997). This interpretation is confirmed by our use of principal component analysis (PCA), which shows neither Ba nor Nb track with PC1, the principal component associated with elements defining a differentiation trend (e.g., Si, Mg, Ca) (see Fig S3) This statistical pattern allows us to explore Ba/Nb systematics further, assured that the signals in Ba/Nb we see are not a function of magmatic differentiation and instead reflect a source process in agreement with previous work. Globally, we ensure this is the case by comparing Ba/Nb to FeOt and MgO in each arc segment; we find that high Ba/Nb contents can be found along both tholeiitic and calc-alkaline differentiation trends (Figure S4).

The complete global patterns in Ba/Nb shown selectively in Figure 1 in the main text are given in Figure S5. As noted in the main text, these plots reveal the underlying structure of Ba/Nb distributions with respect to DTS within each arc. The structures are themselves quite variable, where some arcs show the presence of multiple “peaks” as discussed in Figure 2, while other show very different relationships. For example, the Lesser Antilles subplot shows the presence of only Peak #2 at subarc depths, and minimal fore-arc or back-arc Ba/Nb signals. Other arcs like Mexico or Papua New Guinea show much flatter and less peaked distributions. Other arcs still like Tonga and the Marianas show the presence of all 3 Ba/Nb peaks as discussed in the main text.

Figure S8A and B show binned median values for Th/U and Pb/Nd vs. DTS respectively, with the symbols colored for inter-bin median Ba/Nb. The global arc patterns driving these bins are shown in Figures S9 and S10. As discussed in the main text, these trends in our other indices, Th/U and Pb/Nd, are not as convincing or straightforward as those observed in Ba/Nb. The simple reason behind this is likely because the four elements selected, Th, U, Pb, and Nd all show variable mobility attributed to the stability of many different phases. For example, Th abundances can be directly related to trench sediment, while Pb can be derived from sulfides in the descending oceanic crust. Figures S8-S10 confirm this trend, where higher Ba/Nb contents (the three peaks from Figure 2B) are associated with lower Th/U (higher U) and higher Pb/Nd. The Pb/Nd moving average is at its maximum at subarc depths, and the Th/U moving average is

at its lowest at both subarc and backarc depths (blue regions in Figure S8). We suggest that, as has been argued previously, these FME ratios provide robust estimates of the occurrence and general depths of slab dehydration in subduction zones (Kelley et al., 2005; Pearce et al., 2005; Bebout, 2014); and that there are global systematics in such ratios that are too complex to understand with our global statistical approach.

Lead and U have been found to be similarly mobile in fluid phases in experiments (Kessel et al., 2005; Rustioni et al., 2021) with varying responses to oxidation state and fluid salinity (Rustioni et al., 2021). While U enrichment is commonly associated with fluid components (Elliott et al., 1997; Kelley et al., 2005; Kessel et al., 2005; Schmidt and Poli, 2014), Pb has been suggested to be sourced from destabilized sulphides in addition to hydrous phases in subducted oceanic crust (Walters et al., 2021). We find that Ba/Nb, Th/U and Pb/Nd are not well statistically correlated (Fig. S8, S11). Hence, these elements record different aspects of slab dehydration. Dehydration of altered oceanic crust (AOC) should lead to earlier removal of Pb in the forearc, followed by U at deeper depths, as Pb and U are stored in sulfide and carbonate phases, respectively (Kelley et al., 2005). In contrast, Ba is stored primarily in phengite which is stable up to 300 km during subduction (Kessel et al., 2005; Bebout, 2014; Schmidt and Poli, 2014). Thus, while Th/U and Pb/Nd verify the validity of Ba/Nb as strong signal of slab devolatilisation, at the same time they track multiple different breakdown reactions which are not reflected as clearly as Ba/Nb in the global record.

SUPPLEMENTAL REFERENCES

Bebout, G.E., 2014, 4.20 - Chemical and Isotopic Cycling in Subduction Zones, *in* Holland, H.D. and Turekian, K.K. eds., Treatise on Geochemistry (Second Edition), Oxford, Elsevier, p. 703–747, doi:10.1016/B978-0-08-095975-7.00322-3.

Carter, L.B., Skora, S., Blundy, J.D., De Hoog, J.C.M., and Elliott, T., 2015, An Experimental Study of Trace Element Fluxes from Subducted Oceanic Crust: Journal of Petrology, v. 56, p. 1585–1606, doi:10.1093/petrology/egv046.

Crameri, F., 2018, Scientific colour-maps: Zenodo, v. 10.

Elliott, T., Plank, T., Zindler, A., White, W., and Bourdon, B., 1997, Element transport from slab to volcanic front at the Mariana arc: Journal of Geophysical Research: Solid Earth, v. 102, p. 14991–15019.

Gale, A., Dalton, C.A., Langmuir, C.H., Su, Y., and Schilling, J., 2013, The mean composition of ocean ridge basalts: Geochemistry, Geophysics, Geosystems, v. 14, p. 489–518.

Hayes, G.P., Moore, G.L., Portner, D.E., Hearne, M., Flamme, H., Furtney, M., and Smoczyk, G.M., 2018, Slab2, a comprehensive subduction zone geometry model: Science, v. 362, p. 58 LP – 61, doi:10.1126/science.aat4723.

Hernández-Uribe, D., and Palin, R.M., 2019, A revised petrological model for subducted oceanic crust: Insights from phase equilibrium modelling: Journal of Metamorphic Geology, v. 37, p. 745–768.

Kelley, K.A., Plank, T., Farr, L., Ludden, J., and Staudigel, H., 2005, Subduction cycling of U, Th, and Pb: Earth and Planetary Science Letters, v. 234, p. 369–383.

Kessel, R., Schmidt, M.W., Ulmer, P., and Pettke, T., 2005, Trace element signature of subduction-zone fluids, melts and supercritical liquids at 120–180 km depth: Nature, v. 437, p. 724–727.

Pasyanos, M.E., Masters, T.G., Laske, G., and Ma, Z., 2014, LITHO1.0: An updated crust and lithospheric model of the Earth: Journal of Geophysical Research: Solid Earth, v. 119, p. 2153–2173, doi:10.1002/2013JB010626.

Pearce, J.A., Stern, R.J., Bloomer, S.H., and Fryer, P., 2005, Geochemical mapping of the Mariana arc-basin system: Implications for the nature and distribution of subduction components: Geochemistry, geophysics, geosystems, v. 6.

Rustioni, G., Audétat, A., and Keppler, H., 2019, Experimental evidence for fluid-induced melting in subduction zones: Geochemical Perspectives Letters, v. 11, p. 49–54, doi:10.7185/geochemlet.1925.

Rustioni, G., Audetat, A., and Keppler, H., 2021, The composition of subduction zone fluids and the origin of the trace element enrichment in arc magmas: Contributions to Mineralogy and Petrology, v. 176, p. 51, doi:10.1007/s00410-021-01810-8.

Sarbas, B., and Nohl, U., 2008, The GEOROC database as part of a growing geoinformatics network: Geoinformatics,.

Schmidt, M.W., and Poli, S., 2014, 4.19 - Devolatilization During Subduction, *in* Holland, H.D. and Turekian, K.K. eds., Treatise on Geochemistry (Second Edition), Oxford, Elsevier, p. 669–701, doi:10.1016/B978-0-08-095975-7.00321-1.

Szwillus, W., Afonso, J.C., Ebbing, J., and Mooney, W.D., 2019, Global crustal thickness and velocity structure from geostatistical analysis of seismic data: Journal of Geophysical Research: Solid Earth, v. 124, p. 1626–1652.

Tsay, A., Zajacz, Z., Ulmer, P., and Sanchez-Valle, C., 2017, Mobility of major and trace elements in the eclogite-fluid system and element fluxes upon slab dehydration: Geochimica et Cosmochimica Acta, v. 198, p. 70–91.

Walters, J.B., Cruz-Uribe, A.M., Marschall, H.R., and Boucher, B., 2021, The role of sulfides in the chalcophile and siderophile element budget of the subducted oceanic crust: Geochimica et Cosmochimica Acta, v. 304, p. 191–215, doi:10.1016/j.gca.2021.04.016.

William Pitcher, B., and Kent, A., 2019, Statistics and segmentation: Using Big Data to assess Cascades arc compositional variability: Geochimica et Cosmochimica Acta, doi:https://doi.org/10.1016/j.gca.2019.08.035.

SUPPLEMENTAL FIGURES

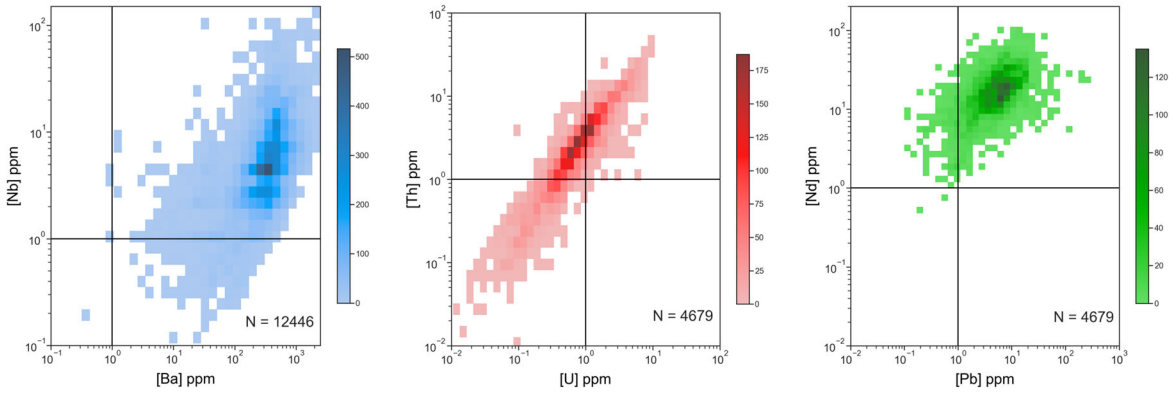

FIGURE S1: Bivariate distribution plots showing a) Ba vs. Nb, b) Th vs. U, and c) Pb vs. Nd. The color of each cell corresponds to the number of samples that have that combination of Element X and Element Y in our global database. Axes are logarithmic for data display purposes.

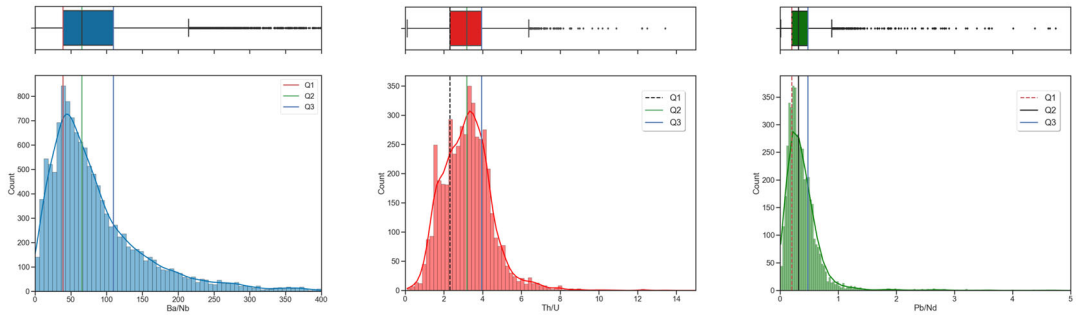

FIGURE S2: Combined histogram and box plots showing the skewed distribution of a) Ba/Nb, b) Th/U, and c) Pb/Nd across our global database. These three metrics each show a strong central

tendency, with most data (defined by the quartiles (Q1, Q2, Q3)) fitting within the interquartile range (IQR).

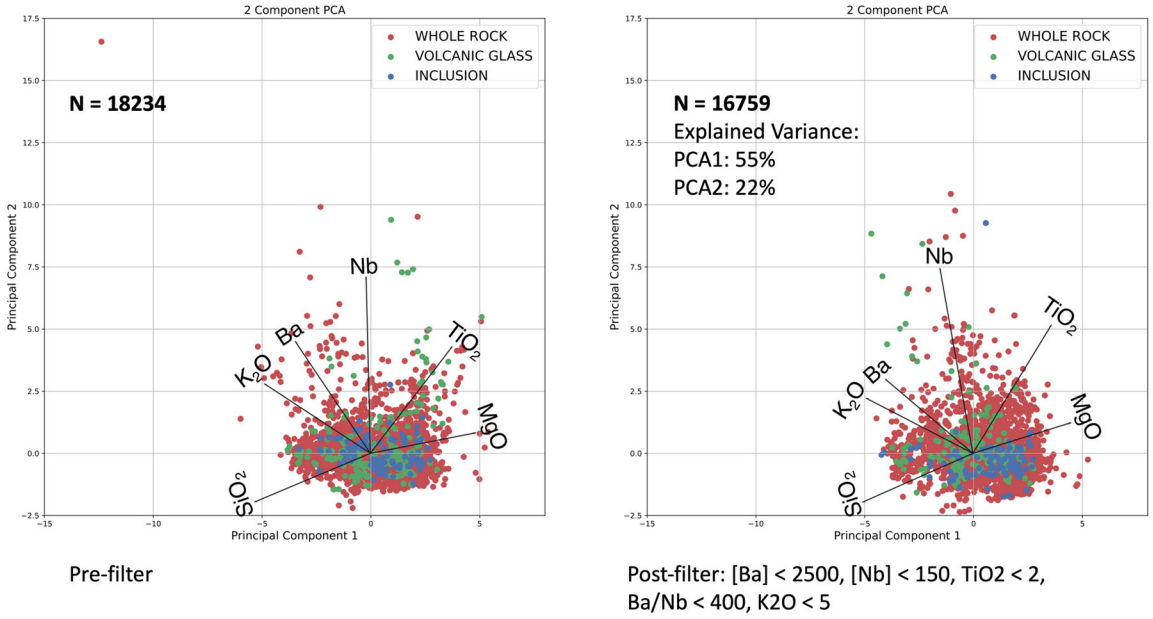

FIGURE S3: Principal Component Analysis (PCA) of several major and trace elements in our global database: SiO2, MgO, TiO2, K2O, Na2O, Ba, and Nb. Axes show the two main principal components, colored for whether the sample in questions comes from a Whole Rock, Glass, or Inclusion measurement (coded originally in GeoRoc). PC1 explains ~ 55% of the variance in our data, while PC2 explains 22% of the variance. Ba and especially Nb are associated with PC2, while all the other elements fall along PC1. Panel (b) represent a PCA analysis with tightly defined filters on our global database tor remove outliers and improve statistical validity: [Ba] < 2500 ppm, [Nb] < 150 ppm, TiO2 < 2 wt.%, Ba.Nb < 400, K2O < 5.

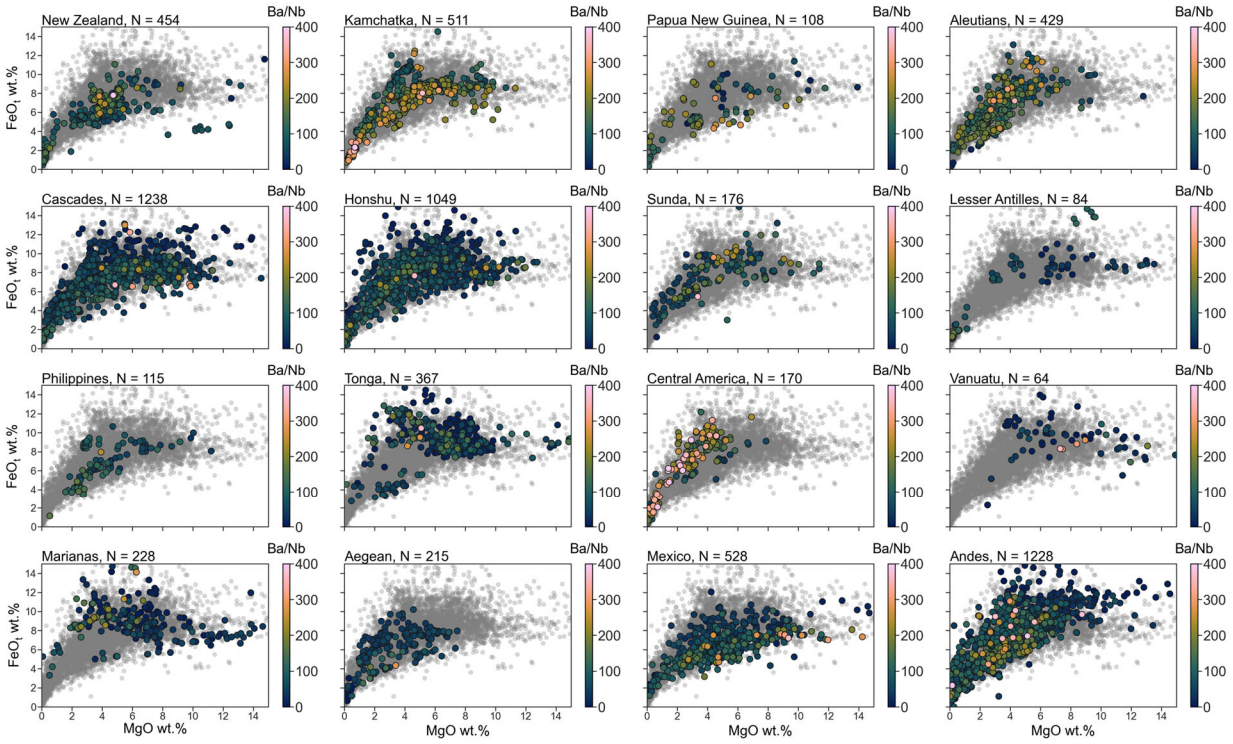

FIGURE S4: Arc-by-arc analysis of FeOt vs. MgO in our global dataset. Each point in a subplot represents the Fe & Mg composition of a sample, colored for the Ba/Nb of that sample using the *Hawaii* color scheme (Crameri, 2018). The number of samples within each arc containing measurable Fe, Mg, Ba, and Nb are shown in the top line above the data points, along with the arc name. Grey points in each subplot background show the global spread of the data.

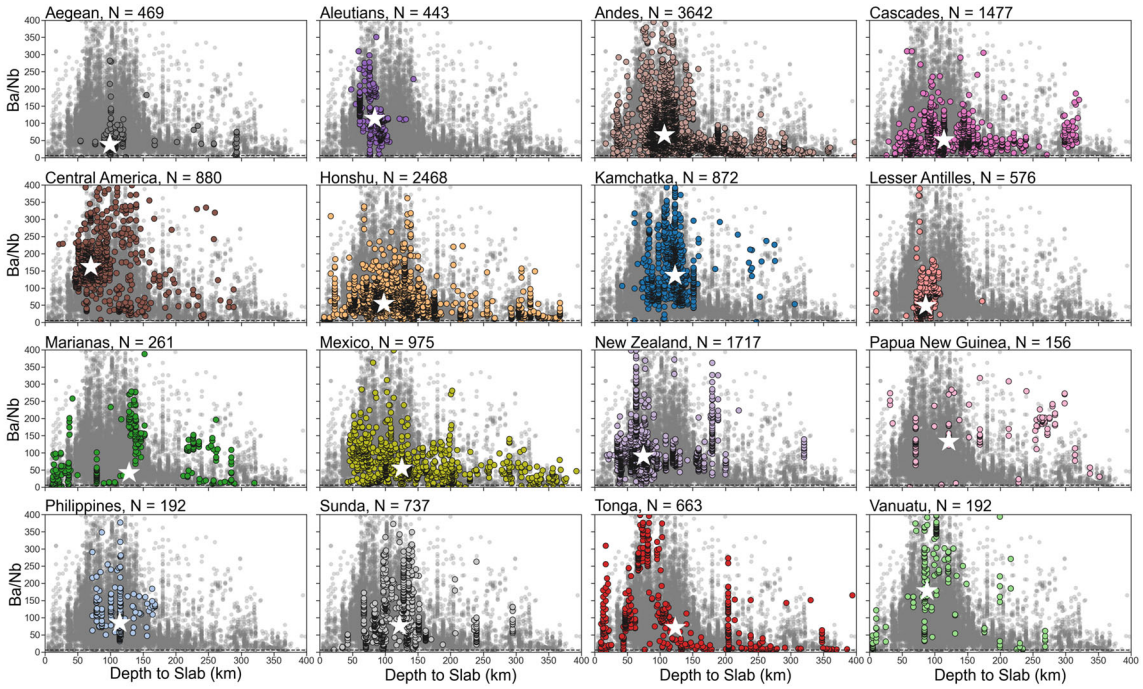

FIGURE S5: Arc-by-arc comparison of Ba/Nb, showing the total number of Ba/Nb measurements within each arc vs. DTS. The white star in each subplot shows the median Ba/Nb as presented in Figures 1E and 1F. The number of samples with Ba/Nb and DTS values within each arc is shown above each subplot along with the arc name. Dashed horizontal line across each subplot shows the N-MORB arithmetic mean Ba/Nb content from Gale et al. 2013.

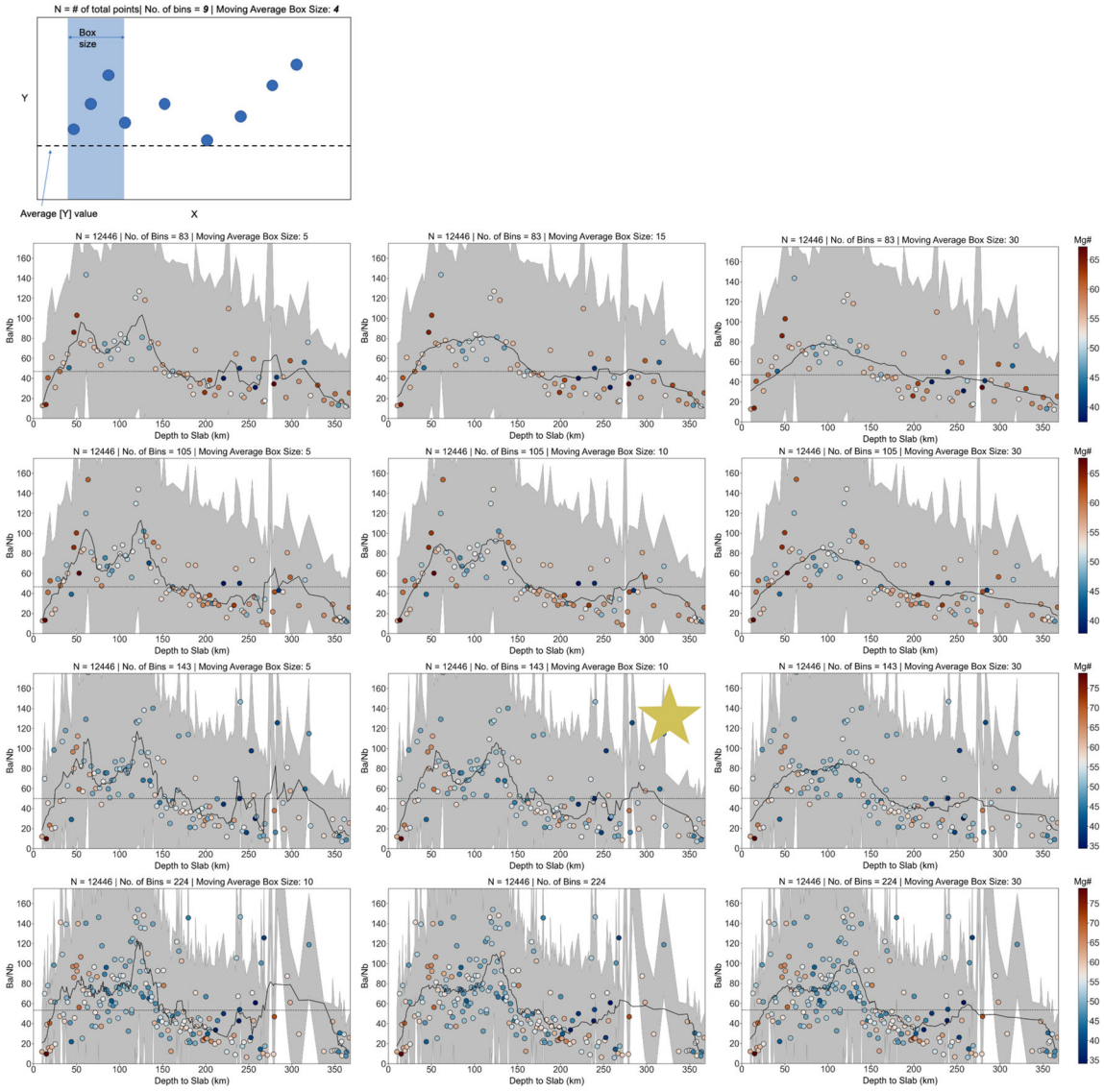

FIGURE S6: Sensitivity analysis showing the effect of varying bin size and box size on our conclusion sin Figure 2B. First panel shows a schematic of the figures, where binning and moving average analyses are defined. In the horizontal direction, the size of the moving average box window is increased moving from the left panel over to the right. In the vertical direction, each new row sees a larger number of bins computed. The panel marked with a yellow star is the panel we report in the main text as Figure 2B. See text for discussion.

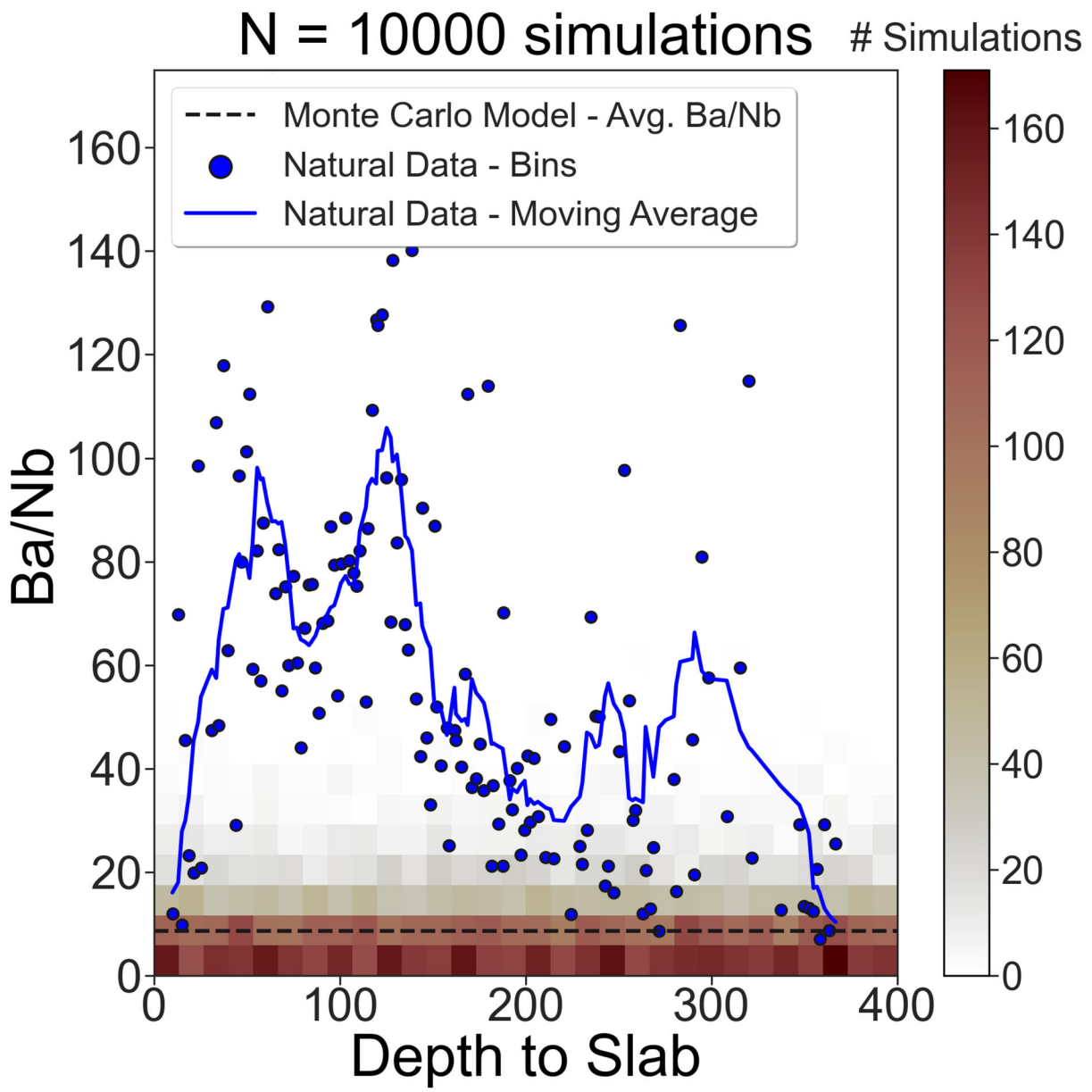

FIGURE S7: Monte Carlo comparison between simulated Ba/Nb and natural Ba/Nb. Monte Carlo methodology discussed in Supplementary Text 1 and 2. Color of 2D histogram bins corresponds to the number of simulated Ba/Nb and DTS contents falling in that range. The same binned median Ba/Nb contents and moving average used in Figure 1C are overlain on these Monte Carlo results and shown as blue circles and a blue line respectively. N = 100000 simulations in a uniform and random parameter space for the Monte Carlo simulations.

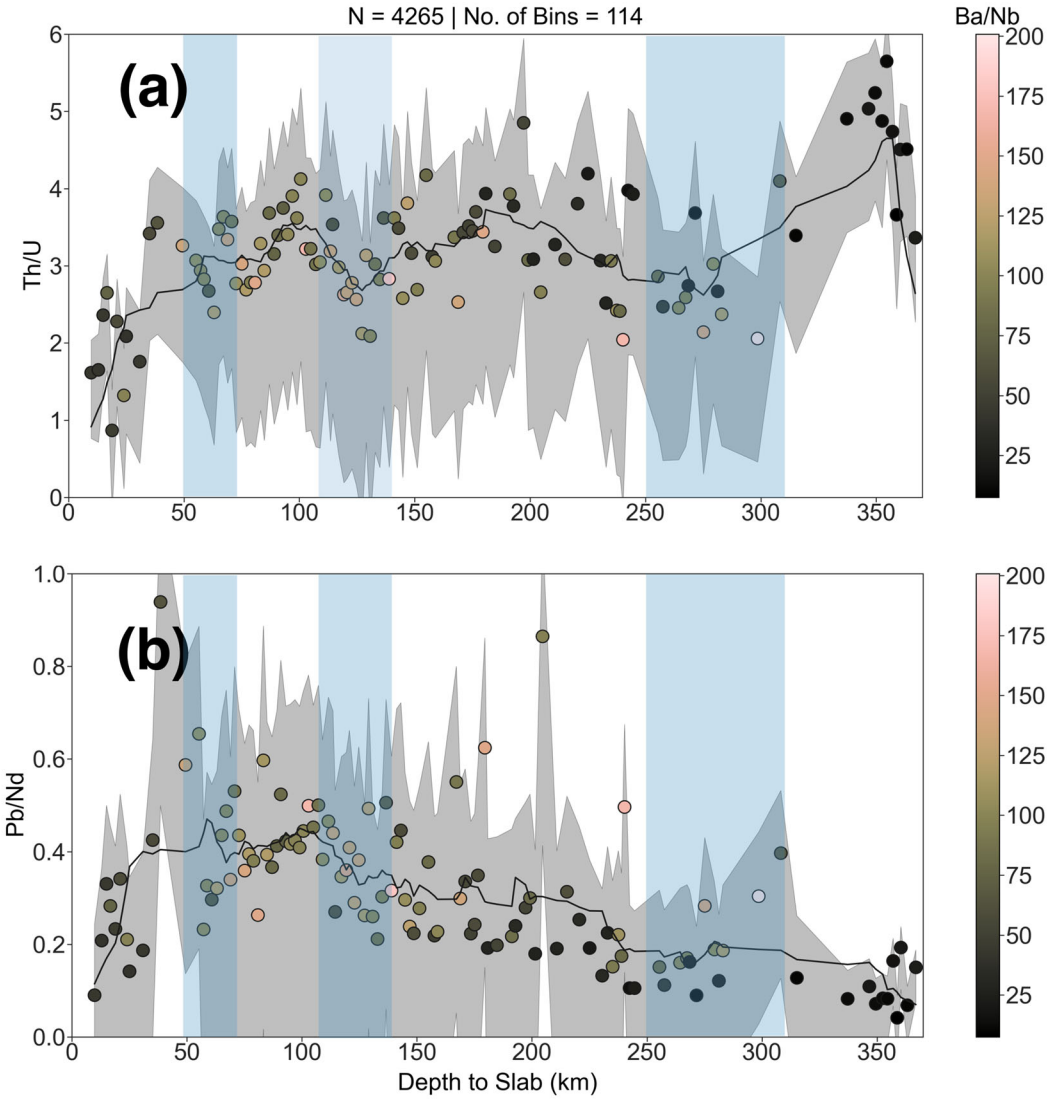

Figure S8: Similar plot style to Figure 2B, showing binned median a) Th/U and b) Pb/Nd. Each binned median for these metrics is shown as a colored circle, with the surrounding grey area representing the 1-σ standard deviation within each bin. The color of each circle corresponds to the median Ba/Nb within each bin. Like 2B, a moving average of the binned median metrics is calculated and shown as a thin black line. The vertical blue bars overlaying the data in both a) and b) represent the approximate positions of the Ba/Nb peaks in 2B.

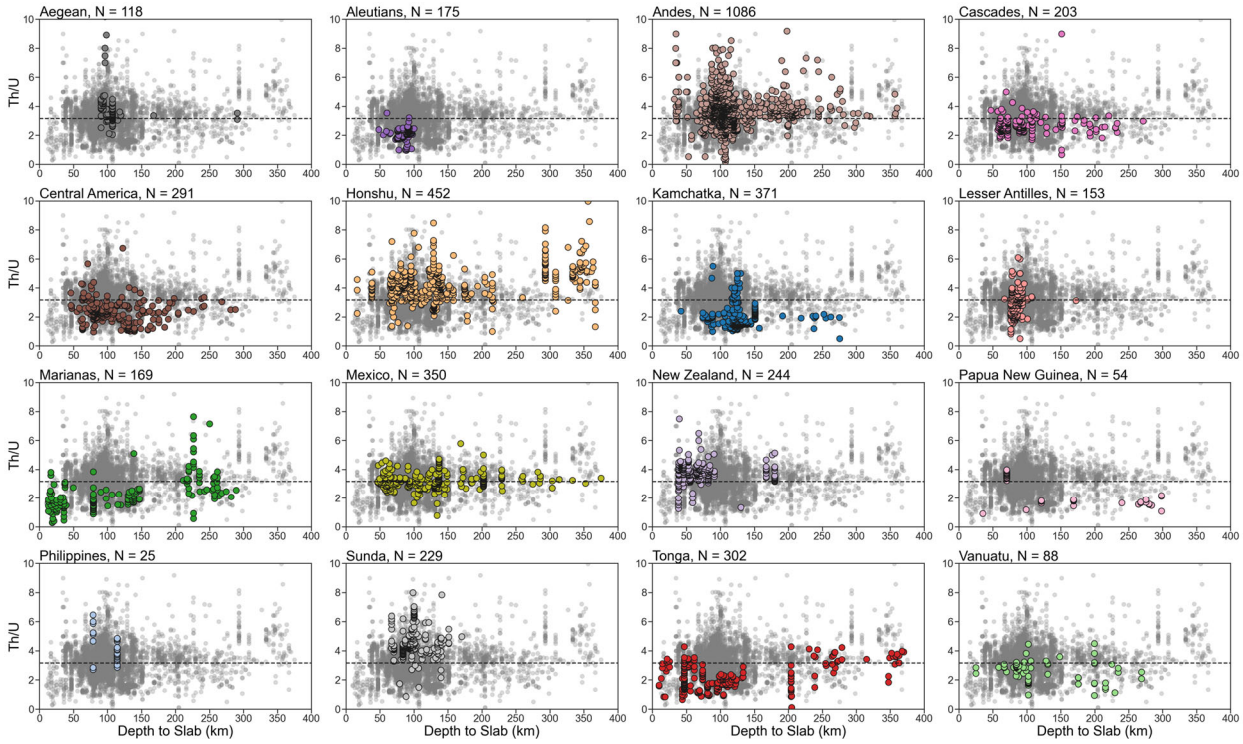

FIGURE S9: Arc-by-arc comparison of Th/U, showing the total number of Th/U measurements within each arc vs. DTS. The number of samples with Th/U and DTS values within each arc is shown above each subplot along with the arc name. Dashed horizontal line across each subplot shows the N-MORB arithmetic mean Th/U content from Gale et al. 2013.

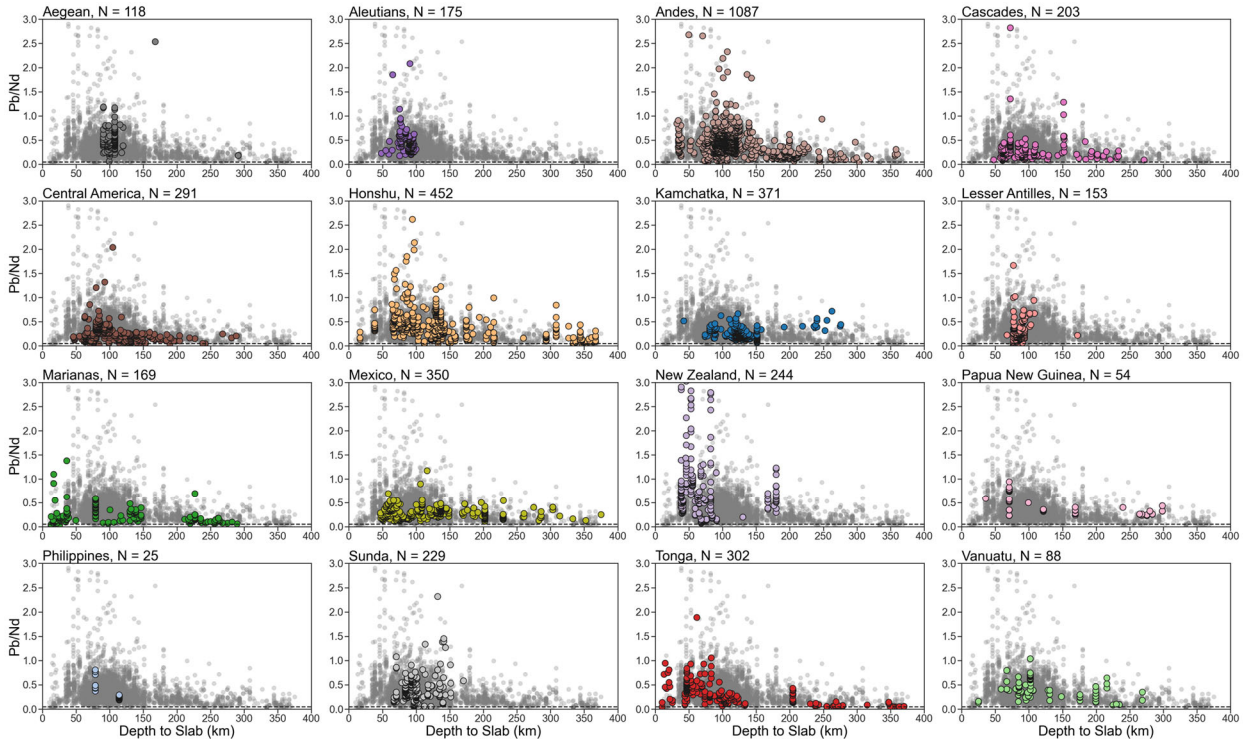

FIGURE S10: Arc-by-arc comparison of Pb/Nd, showing the total number of Pb/Nd measurements within each arc vs. DTS. The number of samples with Pb/Nd and DTS values within each arc is shown above each subplot along with the arc name. Dashed horizontal line across each subplot shows the N-MORB arithmetic mean Pb/Nd content from Gale et al. 2013.

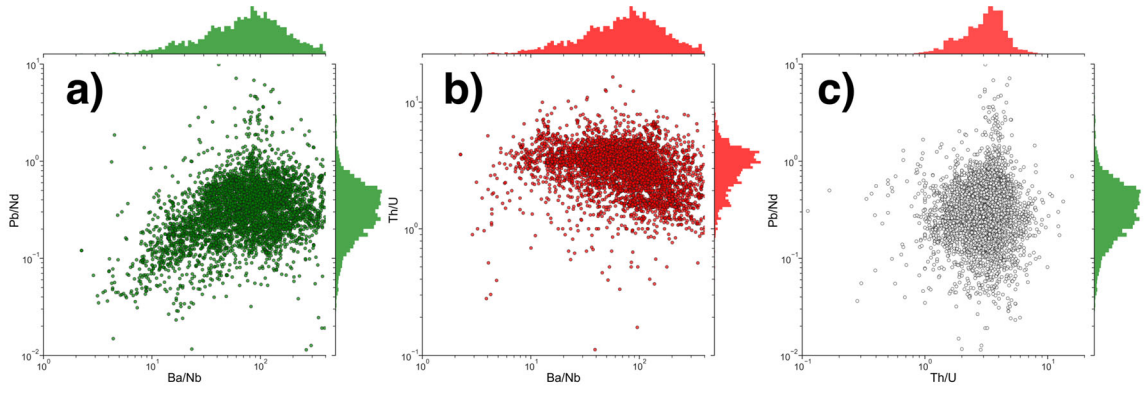

FIGURE S11: Comparative scatter plots showing a) Ba/Nb vs. Th/U, b) Ba/Nb vs. Pb/Nd, c) Th/U vs. Pb/Nd. Each plot shows a kernel density estimate (KDE) distribution of a particular metric on the corresponding axis. Dark lines overlying data points show contours, spaced in 10% increments to show relative density of the datasets.